Energy Materials

Supplementary Material

Fluorine-doped Bi_2O_3 derived from metal-organic framework for electrocatalytic CO_2 reduction to formate at industrial current densities

Yue Qiao, Yue Xu, Junquan Yang, Junfang Ding*, Xiaojun Gu*

School of Chemistry and Chemical Engineering, Inner Mongolia Key Laboratory of Low Carbon Catalysis, Inner Mongolia University, Hohhot 010021, Inner Mongolia, China.

Correspondence to: Dr. Junfang Ding, Dr. Xiaojun Gu, School of Chemistry and Chemical Engineering, Inner Mongolia Key Laboratory of Low Carbon Catalysis, Inner Mongolia University, Hohhot 010021, Inner Mongolia, China. E-mail: dingjf@imu.edu.cn ; xiaojun.gu@imu.edu.cn

Electrochemical measurements

All the electrochemical experiments were conducted using a standard three-electrode system. The data were collected utilizing an electrochemical workstation (CHI1140D, Chenhua, Shanghai, China). In a typical flow cell, the working electrode consisted of hydrophobic carbon paper loaded with catalyst powder, prepared as follows: 5 mg catalyst powder was dispersed in a solution (containing 450 μL ethanol and 50 μL 5 wt% Nafion 117), and sonicated for 1 h to form a catalyst ink. A sample (100 μL) of the resulting ink was dropped onto the hydrophobic carbon paper (1 × 1 cm^{-2}) using a micropipette, achieving a catalyst loading of 1 mg cm^{-2}. The electrode was dried overnight at room temperature. An Ag/AgCl electrode and Pt plate were used as the reference electrode and counter electrode, respectively. A 1 M KOH saturated solution was employed as the electrolyte in all the experiments. The flow rate of CO_2 was controlled at 40 mL min^{-1}, and the catholyte was circulated at a flow rate of 20 standard cubic centimeters per minute (sccm). The linear sweep voltammetry (LSV), cyclic voltammogram (CV), and electrochemical impedance spectroscopy (EIS) tests were conducted under the same conditions.

In the electrochemical tests, all the potentials were referred to a reversible hydrogen

electrode (RHE), applying the equation:

$$E\ (vs.\ RHE) = E\ (vs.\ Ag/AgCl) + 0.197\ V + 0.0591\ V \times pH \quad [1]$$

Product analysis

The gasous products were analyzed using an online gas chromatograph (GC 2014C, Shimadzu) equipped with a thermal conductivity detector (TCD) and a flame ionization detector (FID). The liquid products were quantitatively analyzed using a 600MHZ ^1H NMR spectrometer (Bruker AVANCE NEO) , applying the internal standard method. Typically, 500 μL electrolyte was mixed with100 μL D_2O, and 100 μL DMSO, which was used as an internal standard. The one-dimensional ^1H spectrum was measured with water suppression at the 4.79 peak. The ^1H spectrum peak of formate appeared at ~8.3 and DMSO at ~2.6.

Faradaic efficiency (FE) calculation

The Faradaic efficiency (FE) of a certain gas product was calculated as:

$$FE = \frac{P\,V}{R\,T} \times \frac{v\,N\,F \times 10^{-6}\ (m^3\ mL^{-1})}{I \times 60\ (s\ min^{-1})} \quad [2]$$

v (vol %): volume concentration of certain gas product in the exhaust gas from the cell (GC data);

V: gas flow rate measured by a flow meter;

I: total steady-state cell current;

N: the electron transfer number for certain product formation;

F: Faradaic constant, 96485 C mol^{-1};

R: universal gas constant, 8.314 J mol^{-1} K^{-1};

P: one atmosphere, 1.013×10^5 Pa;

T: room temperature, 298.15 K.

The FE of the liquid products was calculated as:

$$FE = z\ F\ \frac{n}{Q} \quad [3]$$

z: the electron transfer number for per mole of liquid product;

F: Faradaic constant, 96485 C mol^{-1};

n: the content of liquid products determined from NMR (mole);

Q: the total amount of charge passed through the cathode (A·s).

ECSA calculations

The electrochemical surface area (ECSA) was determined in double-layer capacitance (Cdl) measurements using cyclic voltammetry (CV)[4]. The CV scans were performed in a non-Faradaic potential window at various scan rates (10-50 mV s^{-1}). The current density ($\Delta j = ja - jc$) at a designated potential was plotted a function of scan rate, where the slope corresponds to twice the double-layer capacitance (Cdl).

The ECSA was calculated using the equation:

$$ECSA = Cdl / Cs$$

Cdl: the double-layer capacitance obtained from CV measurements

Cs: the specific capacitance; a standard value of 60 μF cm^{-2} was employed for metal oxide electrodes in an alkaline electrolyte

Tafel Slope calculations

The kinetics of the electrocatalytic reaction were evaluated using the Tafel slope, which was derived from the linear sweep voltammetry (LSV) polarization curves.The overpotential (η) was calculated and plotted as a function of the logarithm of the current density (log |j|). The Tafel slope was determined from the linear region of this plot by performing a linear fit according to the classical Tafel equation ($\eta = b \cdot \log (j / j_0)$). A lower Tafel slope value indicates more favorable reaction kinetics for the electrochemical process.

Computational details

All the DFT calculations were implemented, applying the Perdew-Burke-Ernzerh (PBE) generalized gradient approximation (GGA) exchange-correlation functional using the Vienna ab initio simulation package (VASP) code[5,6]. The projector augmented wave (PAW) method was applied to describe the core-valence interaction, and the valence electronic structures of all the atoms were expanded on a set of plane waves with a cut off energy of 450 eV[7]. The electronic relaxation for self-consistency was set at 10^{-6} eV, and the residual forces were limited to less than 0.01 eV $Å^{-1}$. A Monkhorst-Pack k-point

mesh (3 ×3 × 1) grid was used in the calculations.

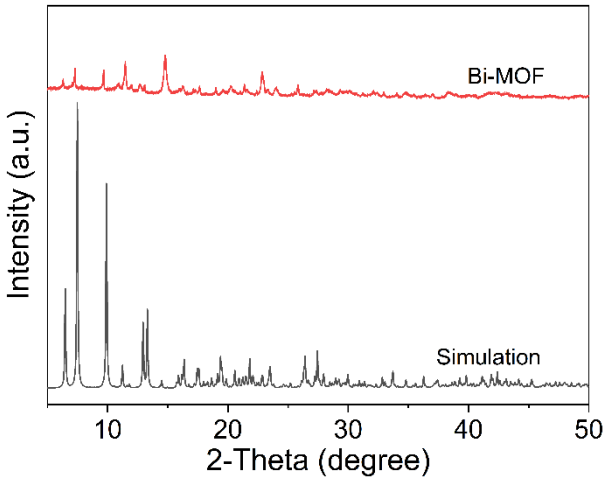

Supplementary Figure 1. XRD pattern of Bi-MOF.

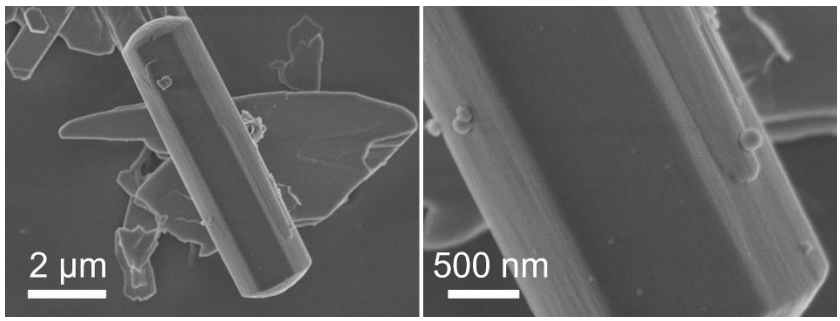

Supplementary Figure 2. SEM images of Bi-MOF at different scales.

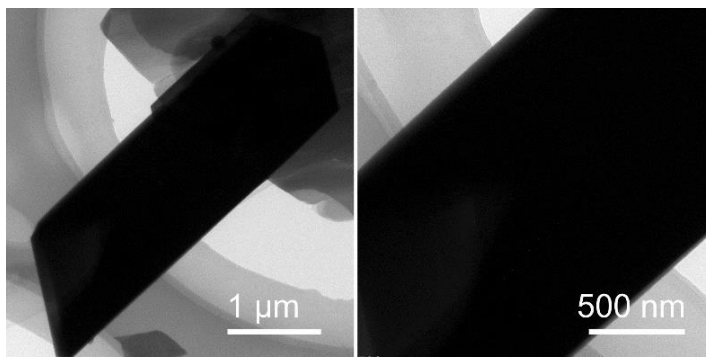

Supplementary Figure 3. TEM images of Bi-MOF at different scales.

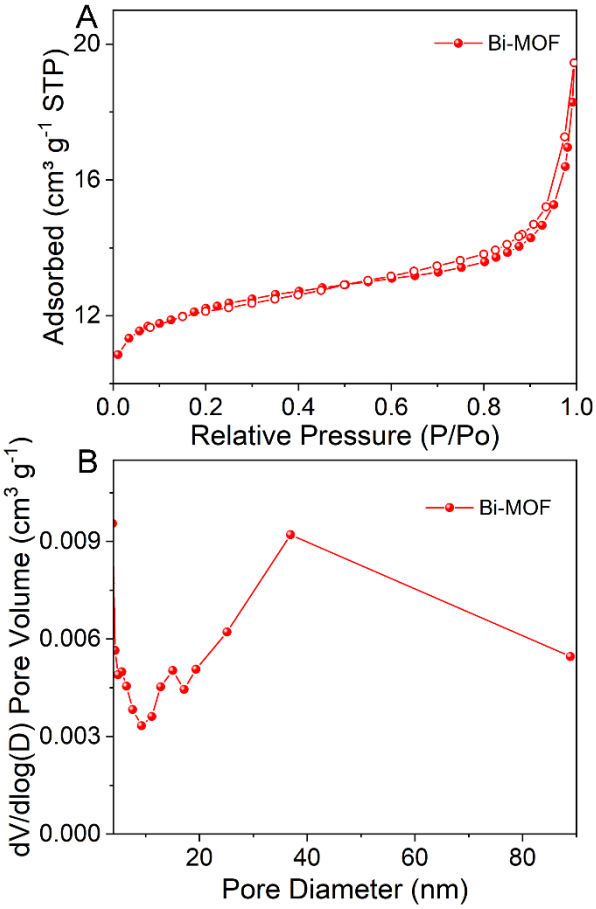

Supplementary Figure 4. (A) Nitrogen adsorption-desorption isotherm and (B) the pore size distribution curve of Bi-MOF.

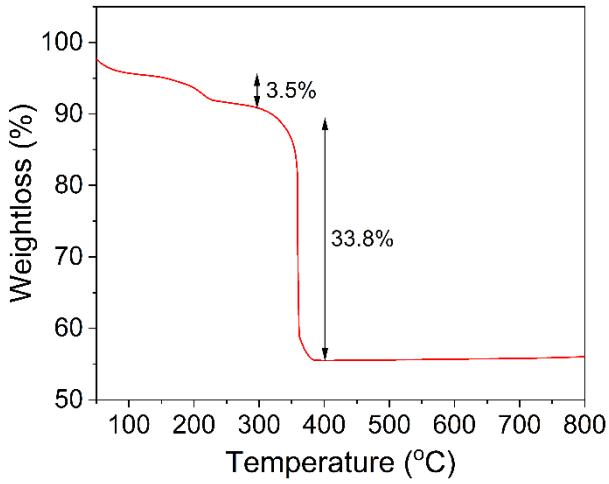

Supplementary Figure 5. TGA curve of Bi-MOF.

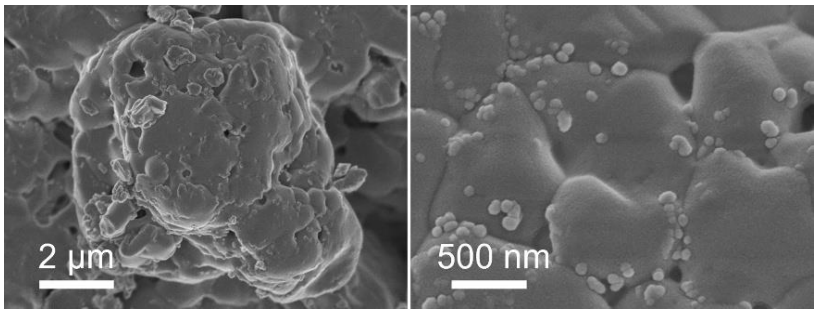

Supplementary Figure 6. SEM images of Bi_2O_3 at different scales.

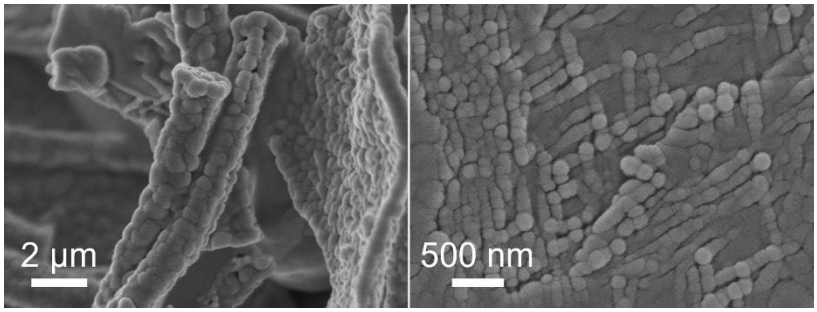

Supplementary Figure 7. SEM images of Bi_2O_3-O_v at different scales.

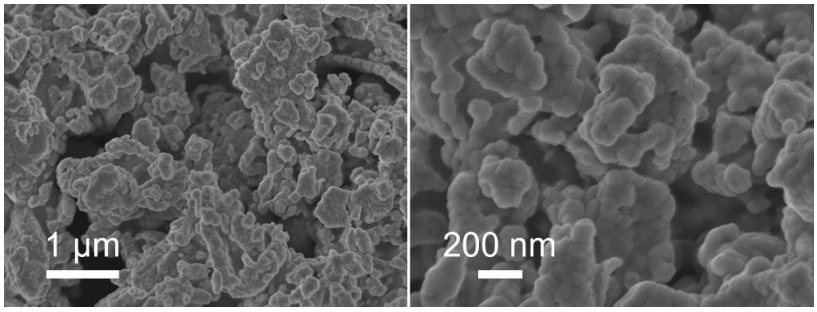

Supplementary Figure 8. SEM images of F-Bi_2O_3-O_v at different scales.

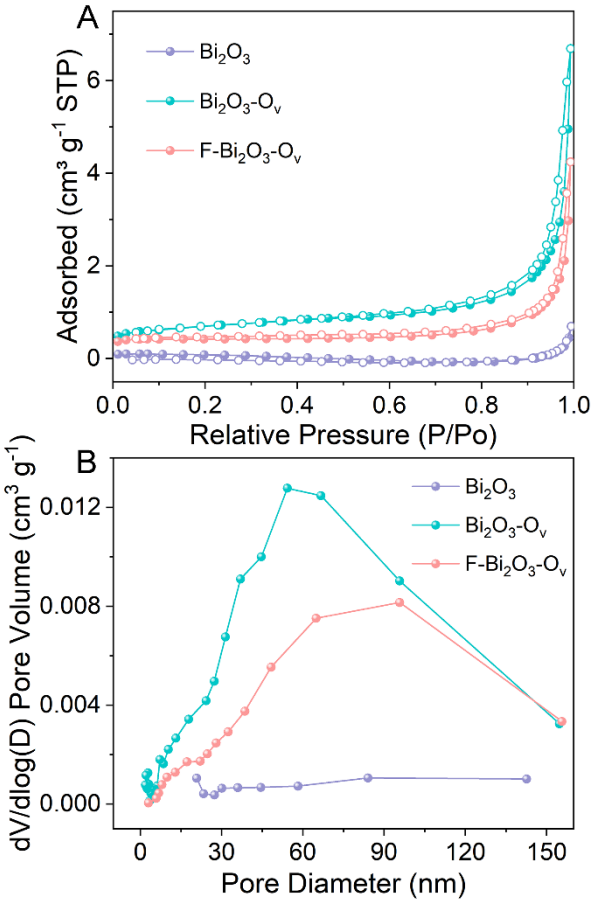

Supplementary Figure 9. (A) Nitrogen adsorption-desorption isotherms and (B) the pore size distribution curves of Bi_2O_3, Bi_2O_3-O_v and F-Bi_2O_3-O_v.

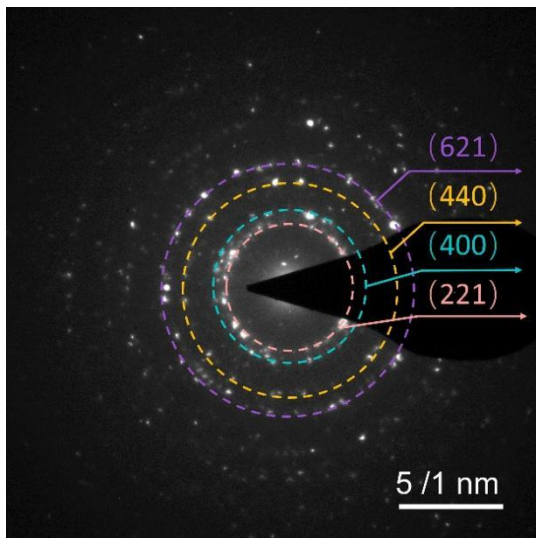

Supplementary Figure 10. SAED pattern of Bi_2O_3-O_v.

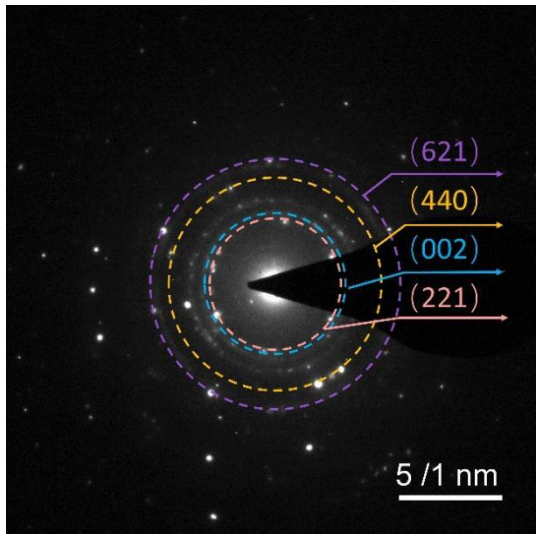

Supplementary Figure 11. SAED pattern of F-Bi_2O_3-O_v.

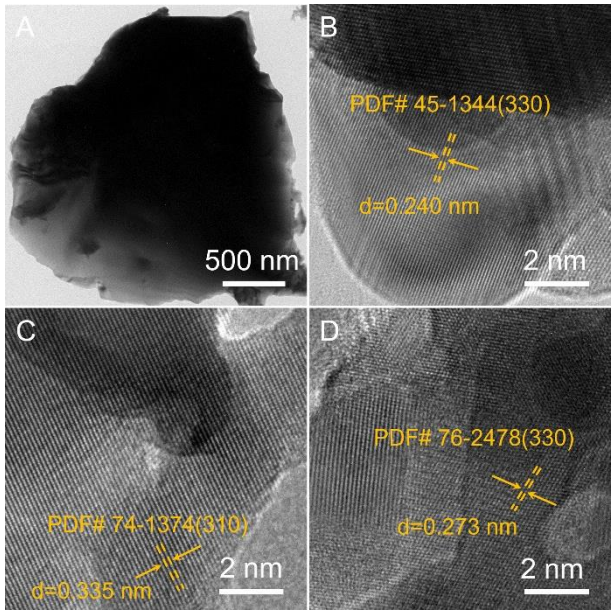

Supplementary Figure 12. (A) TEM and (B-D) HRTEM images of Bi_2O_3.

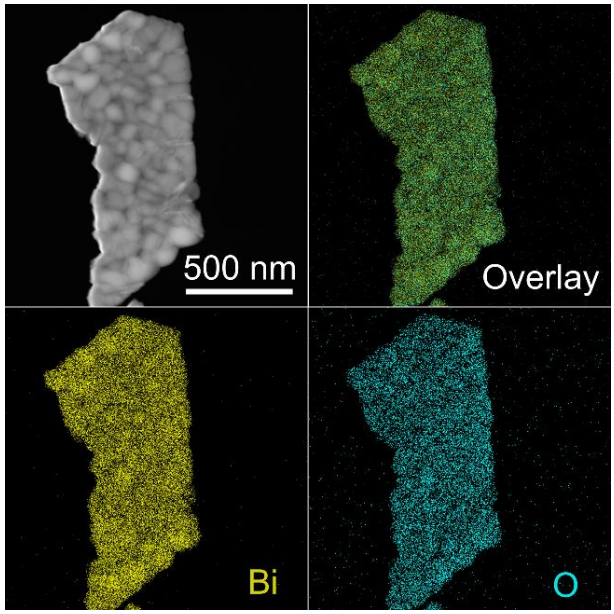

Supplementary Figure 13. Elemental mapping images of Bi_2O_3-O_v.

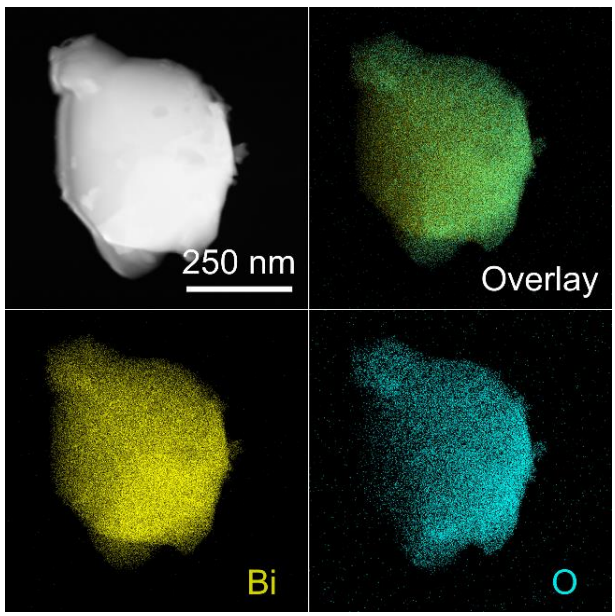

Supplementary Figure 14. Elemental mappings of Bi_2O_3.

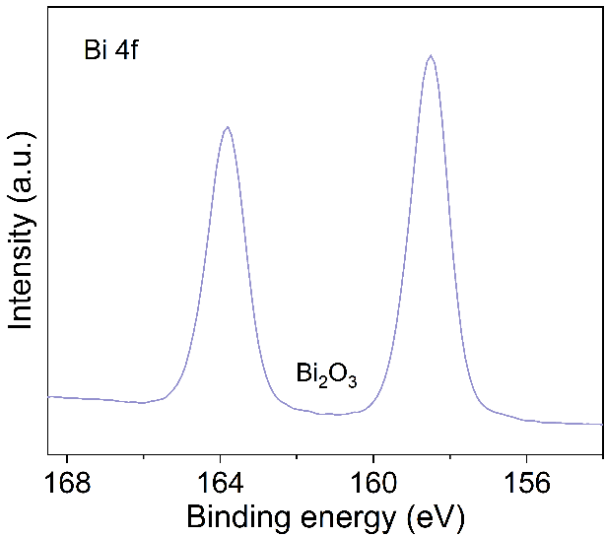

Supplementary Figure 15. XPS spectrum of Bi 4f for Bi_2O_3.

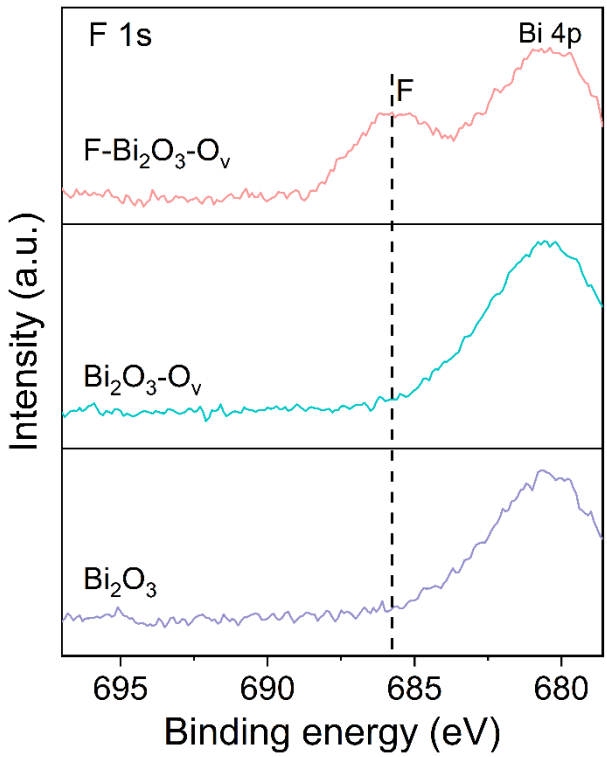

Supplementary Figure 16. XPS spectra of F 1s for Bi_2O_3, Bi_2O_3-O_v and F-Bi_2O_3-O_v.

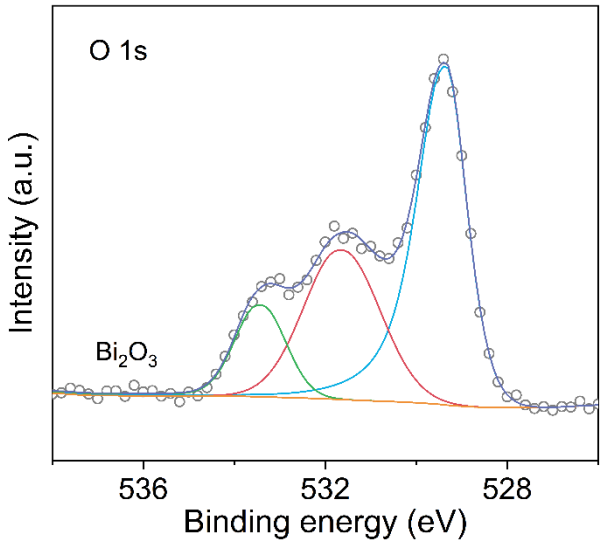

Supplementary Figure 17. XPS spectra of O 1s for Bi_2O_3.

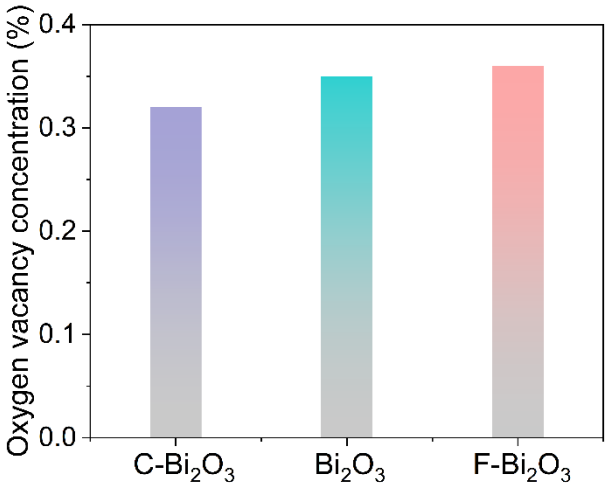

Supplementary Figure 18. Content of O_v for Bi_2O_3, Bi_2O_3-O_v and F-Bi_2O_3-O_v.

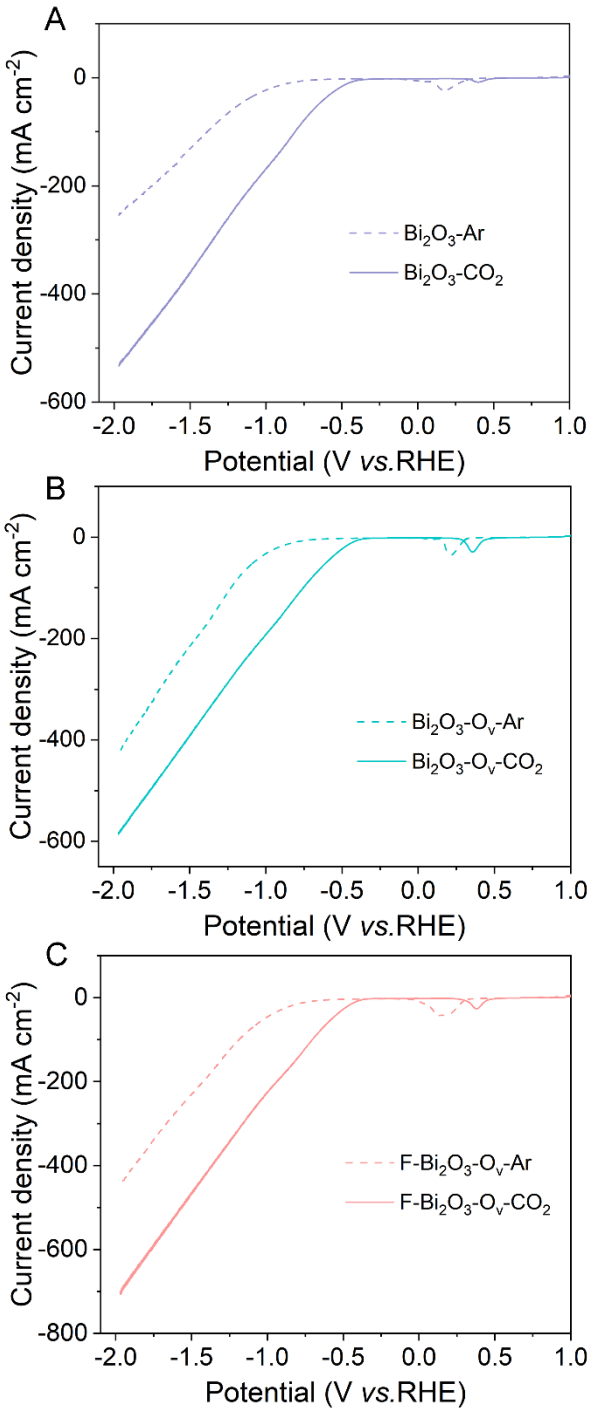

Supplementary Figure 19. LSV curves of (A) Bi_2O_3, (B) Bi_2O_3-O_v and (C) F-Bi_2O_3-O_v in the Ar or CO_2-saturated 1 M KOH electrolyte at a scan rate of 50 mV s^{-1}.

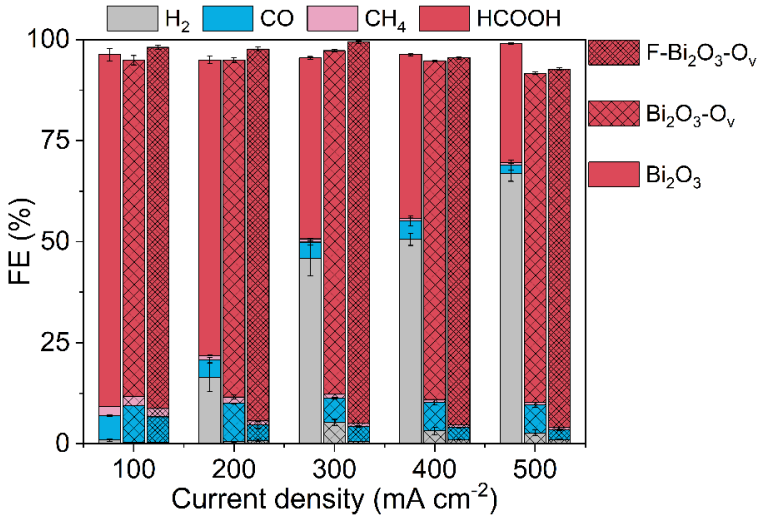

Supplementary Figure 20. Faradaic efficiencies of reduction products for Bi_2O_3, Bi_2O_3-O_v and F-Bi_2O_3-O_v.

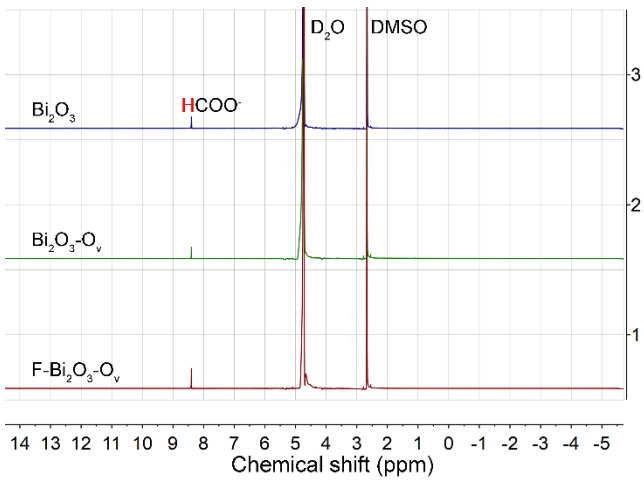

Supplementary Figure 21. ^1H NMR spectra of the electrolytes after CO_2 electroreduction at a current of 300 mA conducted with Bi_2O_3, Bi_2O_3-O_v and F-Bi_2O_3-O_v. DMSO is used as an internal standard for quantification of liquid products.

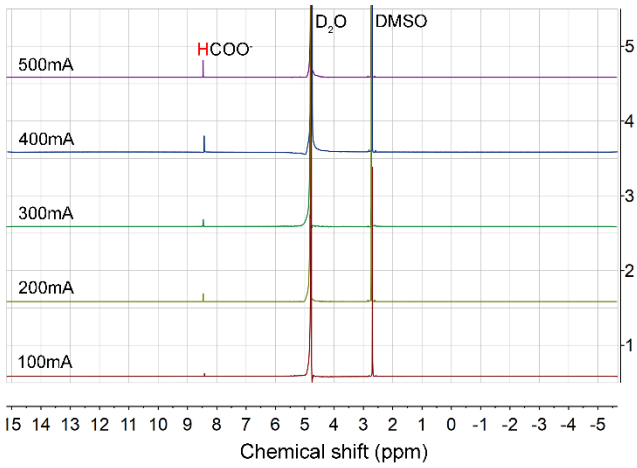

Supplementary Figure 22. Current-dependent ^{1}H NMR spectra of the electrolytes after CO_2 electroreduction for the F-Bi_2O_3-O_v, DMSO is used as an internal standard for quantification of liquid products.

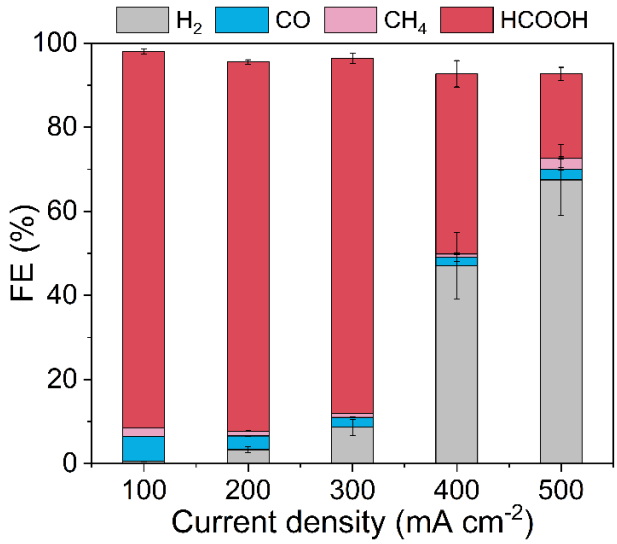

Supplementary Figure 23. Faradaic efficiency of reduction products for F-Bi_2O_3.

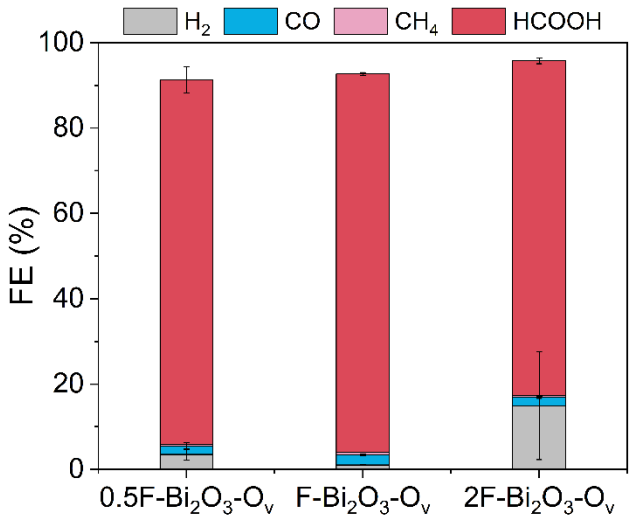

Supplementary Figure 24. Faradaic efficiencies of reduction products for 0.5F-Bi_2O_3-O_v, F-Bi_2O_3-O_v and 2F-Bi_2O_3-O_v.

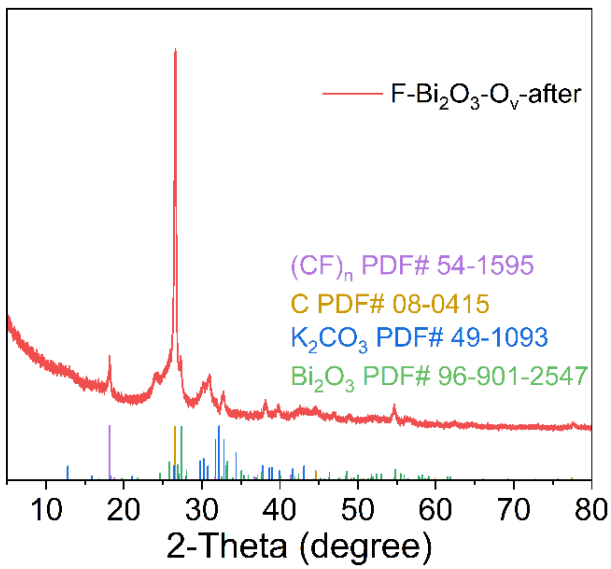

Supplementary Figure 25. XRD pattern of F-Bi_2O_3-O_v after the stability test.

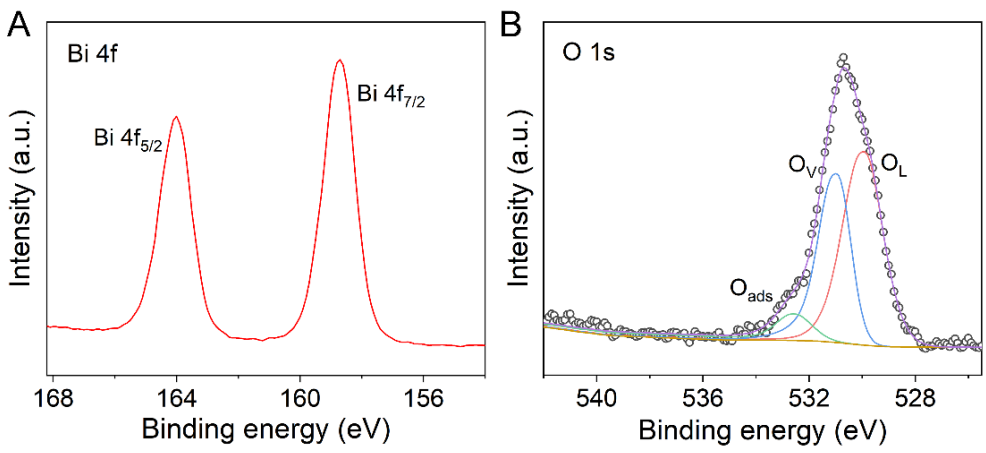

Supplementary Figure 26. XPS spectra of (A) Bi 4f and (B) O 1s for the used F-Bi_2O_3-O_v.

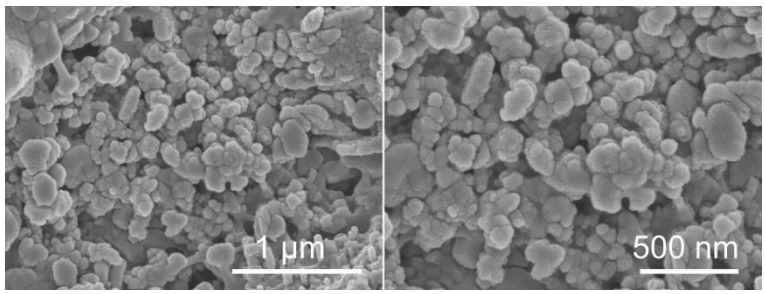

Supplementary Figure 27. SEM images of F-Bi_2O_3-O_v after electrochemical test.

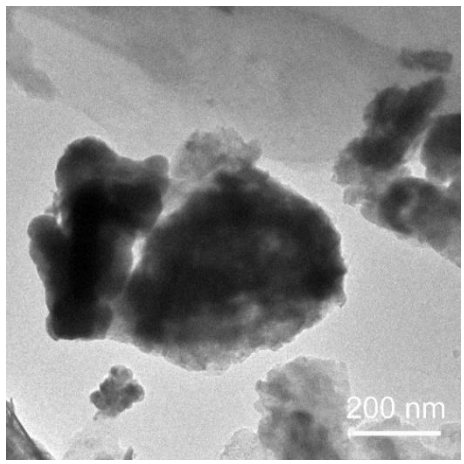

Supplementary Figure 28. TEM image of F-Bi_2O_3-O_v after electrochemical test.

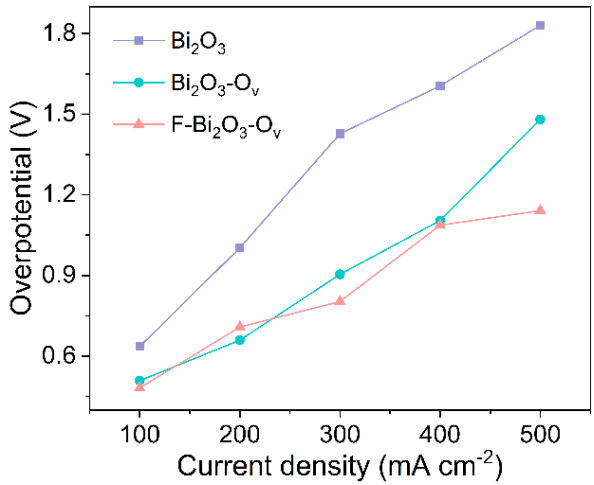

Supplementary Figure 29. Overpotential plots of Bi_2O_3, Bi_2O_3-O_v and F-Bi_2O_3-O_v.

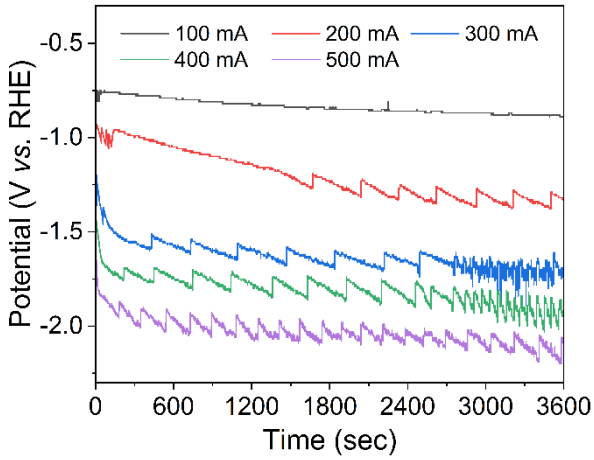

Supplementary Figure 30. Representative chronopotentiometric curves of Bi_2O_3 at different constant current densities.

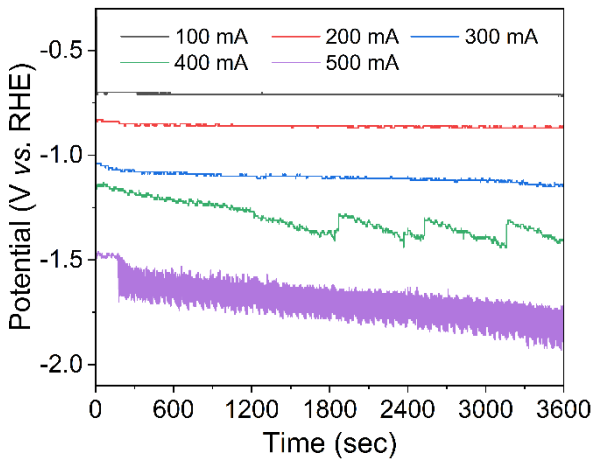

Supplementary Figure 31. Representative chronopotentiometric curves of Bi_2O_3-O_v at different constant current densities.

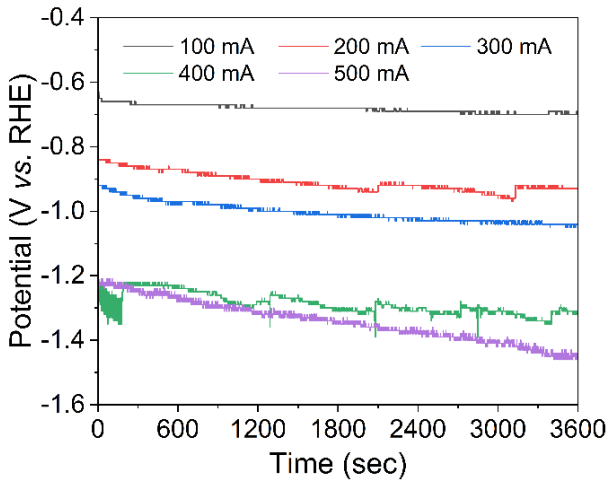

Supplementary Figure 32. Representative chronopotentiometric curves of F-Bi_2O_3-O_v at different constant current densities.

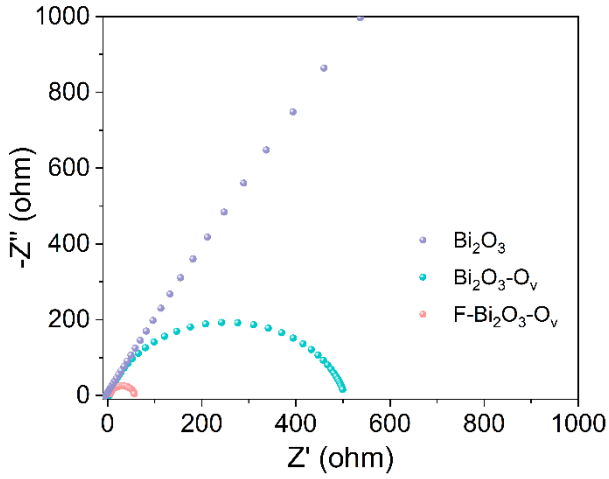

Supplementary Figure 33. Nyquist plots of Bi_2O_3, Bi_2O_3-O_v and F-Bi_2O_3-O_v.

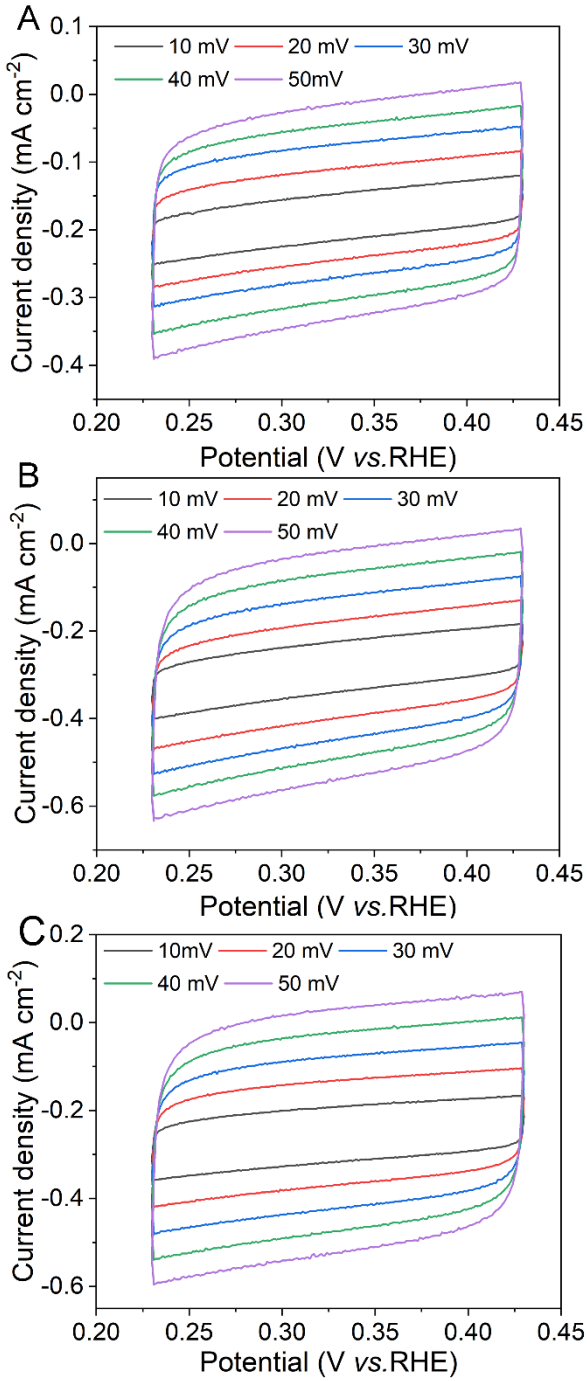

Supplementary Figure 34. CV curves with various scan rates of (A) Bi_2O_3, (B) Bi_2O_3-O_v and (C) F-Bi_2O_3-O_v.

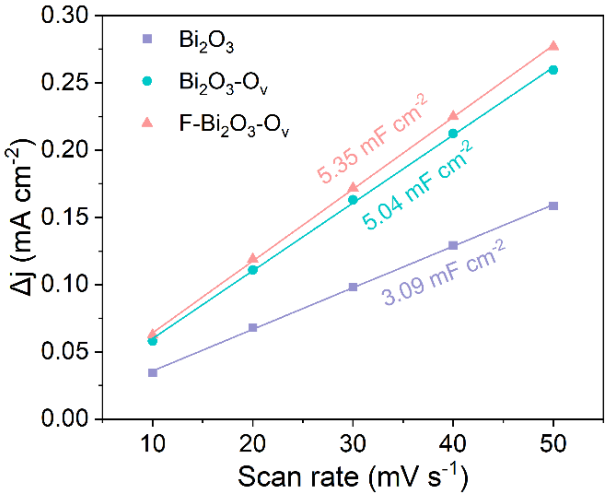

Supplementary Figure 35. Electrochemical double layer capacitances of Bi_2O_3, Bi_2O_3-O_v and F-Bi_2O_3-O_v.

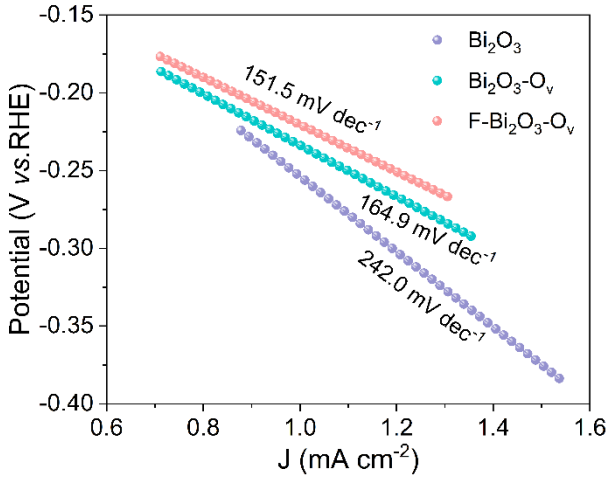

Supplementary Figure 36. Tafel plots of Bi_2O_3, Bi_2O_3-O_v and F-Bi_2O_3-O_v.

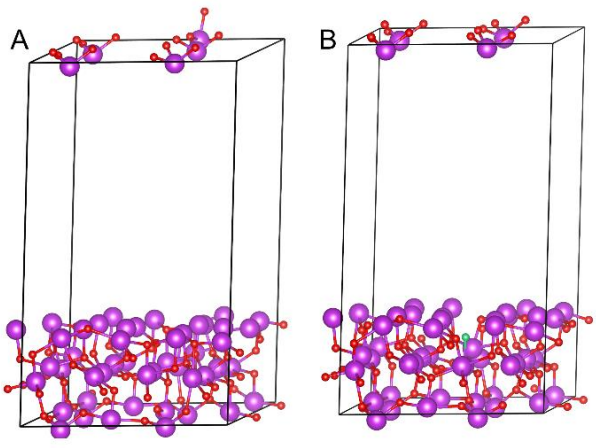

Supplementary Figure 37. Optimized theoretical models of (a) Bi_2O_3-O_v and (b) F-Bi_2O_3-O_v (purple: Bi, red: O, green: F).

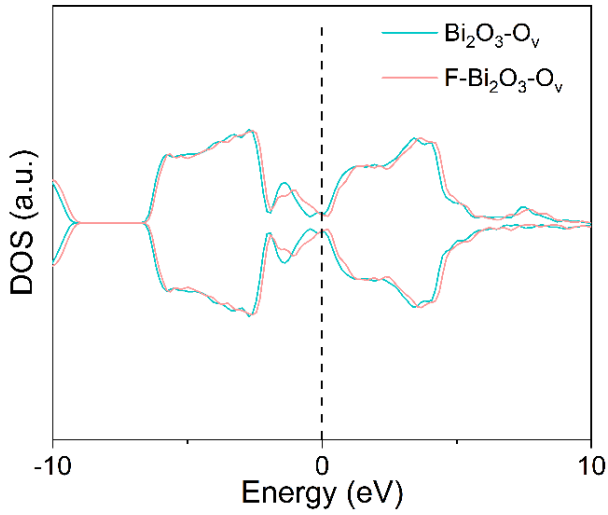

Supplementary Figure 38. DOS of Bi_2O_3-O_v and F-Bi_2O_3-O_v.

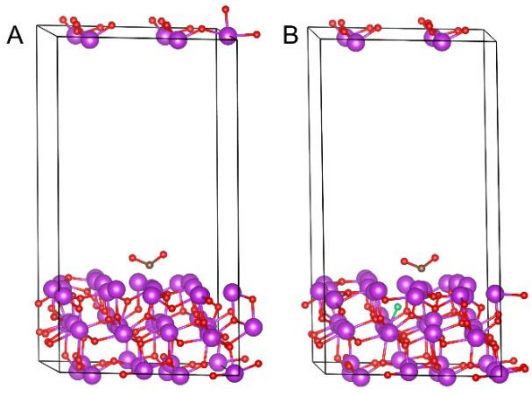

Supplementary Figure 39. Side views of the *CO_2 adsorption models for (a) Bi_2O_3-O_v and (b) F-Bi_2O_3-O_v (purple: Bi, red: O, green: F, white: H, brown: C).

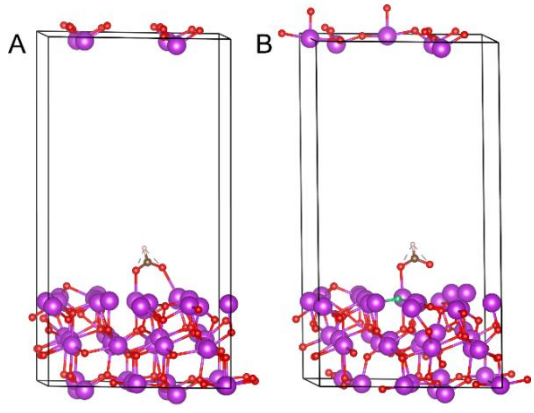

Supplementary Figure 40. Side views of the *OCHO adsorption models for (A) Bi_2O_3-O_v and (B) F-Bi_2O_3-O_v ((purple: Bi, red: O, green: F, white: H, brown: C).

Supplementary Table 1. Comparison of Bi-based materials electrocatalytic performances of ECO_2R to formate in flow cells with 1M KOH electrolyte

Sample	J ($mA\ cm^{-2}$)	Potential (V *vs*. RHE)	$FE_{formate}$ (%)	Stability (h)	Ref.
F-Bi_2O_3-O_v	443	-0.8	94	25	This work
In-Bi_2O_3	407.5	-1.2	91.1	25	[8]
V-Bi NS	400	-0.8	95	30	[9]
Bi_2O_3@C-800	150	-0.9	93	1	[10]
JUC-626-Bi-TR	350	-1	97.1	24	[11]
BiS-1	300	-0.9	95	16	[12]
$Bi_2O_2CO_3$/Bi	543	-1.43	93.68	10	[13]
$Bi_{19}Br_3S_{27}$	200	-0.95	95	3.33	[14]

REFERENCES

1. Wang, X.; Zhang, Y.; Wang, S.; et al. Steering geometric reconstruction of bismuth with accelerated dynamics for CO_2 electroreduction. *Angew. Chem. Int. Ed.* **2024**, *63*, e202515485. DOI: 10.1002/anie.202407665
2. Yi, J.; Gao, X.; Zhou, H.; et al. Design of Co-Cu diatomic site catalysts for high-efficiency synergistic CO_2 electroreduction at industrial-level current density. *Angew. Chem. Int. Ed.* **2022**, *61*, e202212329. DOI: 10.1002/anie.202212329
3. Xu, F.; Feng, B.; Shen, Z.; et al. Oxygen-bridged Cu binuclear sites for efficient electrocatalytic CO_2 reduction to ethanol at ultralow overpotential. *J. Am. Chem. Soc.* **2024**, *146*, 9365-9374. DOI: 10.1021/jacs.4c01610
4. Chen, C.; Yan, X.; Liu, S.; et al. Highly efficient electroreduction of CO_2 to C_{2+} alcohols on heterogeneous dual active sites. *Angew. Chem. Int. Ed.* **2020**, *59*, 16459-16464. DOI: 10.1002/anie.202006847
5. Perdew, J. P.; Burke, K.; Ernzerhof, M.; et al. Generalized gradient approximation made simple. *Phys. Rev. Lett.* **1996**, *77*, 3865. DOI: 10.1103/physrevlett.77.3865
6. Kresse, G.; Furthmu¨ller, J. Efficient iterative schemes for ab initio total-energy calculations using a plane-wave basis set. *Phys. Rev. B* **1996**, *54*, 11169-11186. DOI: 10.1103/physrevb.54.11169
7. Blöchl, P. E. Projector augmented-wave method. *Phys. Rev. B* **1994**, *50*, 17953-17979. DOI: 10.1103/PhysRevB.50.17953
8. Wang, J.; Tang, W.; Zhu, Z.; et al. Stabilizing lattice oxygen of Bi_2O_3 by interstitial insertion of indium for efficient formic acid electrosynthesis. *Angew. Chem. Int. Ed.* **2025**, *64*, e202423658. DOI: 10.1002/anie.202423658

9. Wang, X.; Zhang, Y.; Wang, S.; et al. Steering geometric reconstruction of bismuth with accelerated dynamics for CO_2 electroreduction. *Angew. Chem. Int. Ed.* **2024**, *63*, e202407665. DOI: 10.1002/anie.202407665
10. Deng, P.; Yang, F.; Wang, Z.; et al. Metal-organic framework-derived carbon nanorods encapsulating bismuth oxides for rapid and selective CO_2 electroreduction to formate. *Angew. Chem. Int. Ed.* **2020**, *59*, 10807-10813. DOI: 10.1002/anie.202000657
11. Zhang, Z.; Zhang, Z.; He, J.; et al. Stabilizing highly active metastable Bi (101) facet via covalent organic frameworks to break activity-stability trade-off in CO_2-to-HCOOH electrocatalysis. *Angew. Chem. Int. Ed.* **2025**, *64*, e202515485. DOI: 10.1002/anie.202515485
12. Jiang, Z.; Ren, S.; Cao, X.; et al. pH-universal electrocatalytic CO_2 reduction with ampere-level current density on doping-engineered bismuth sulfide. *Angew. Chem. Int. Ed.* **2024**, *63*, e202408412. DOI: 10.1002/anie.202408412
13. Liu, X.; Zheng, H.; Sun Q.; et al. Mastering the lattice strain in bismuth-based electrocatalysts for efficient CO_2-to-formate conversion. *Adv. Funct. Mater.* **2024**, *34*, 2400928. DOI: 10.1002/adfm.202400928
14. Lv, L.; Lu, R.; Zhu, J.; et al. Coordinating the edge defects of bismuth with sulfur for enhanced CO_2 electroreduction to formate. *Angew. Chem. Int. Ed.* **2023**, *62*, e202303117. DOI: 10.1002/anie.202303117